Impacts of the assimilation of satellite sea surface temperature data on estimates of the volume and heat budgets of the North Sea

W. Chen[1], J. Schulz-Stellenfleth[1], S. Grayek[1], and J. Staneva[1]

[1]Institute of Coastal Research, Helmholtz-Zentrum Geesthacht (HZG), Max-Planck-Str. 1, 21502 Geesthacht, Germany

Key Points:

- Besides the impacts on the temperature, the sea surface temperature assimilation further affects the remaining prognostic model variables.
- The sea surface temperature assimilation reduces lateral volume and heat transport from the Atlantic to the North Sea.
- The sea surface temperature assimilation enhances air-sea heat exchange and alongshelf current at the northern edge of the North Sea.

Corresponding author: W. Chen, wei.chen@hzg.de

Abstract

The different mechanisms controlling the heat budget of the North Sea are investigated based on a combination of satellite sea surface temperature measurements and numerical model simulations. Lateral heat fluxes across the shelf edge and into the Baltic Sea are considered, as well as vertical ocean-atmosphere heat exchange. The 3DVAR data assimilation (DA) scheme is applied, which contains assumed model error correlations depending on the mixed layer depth derived from a coupled circulation/ocean wave model. The simulated seawater temperature is improved both at the surface and at greater water depths. DA is shown to change the current velocity field and decrease the lateral advective volume/heat exchanges between the North Sea and the Atlantic, yielding an increased heat flux from the Atlantic into the North Sea and more heat flux from the sea to the atmosphere. The largest DA impact on volume/heat transport is found at the Norwegian Channel, where the dominant process is Eulerian transport, followed by tidal pumping and wind pumping, while other processes, such as Stokes transport, transport driven by the annual mean wind stress, and tide-wind interactions, are negligible. Further analysis reveals the acceleration of the along-shelf current at the northern edge of the North Sea and a decrease in the horizontal pressure gradient from the Atlantic to the North Sea. DA changes the velocity field inside the Norwegian Channel and the instability of the water column, which in turn reduces the Eulerian transport of heat and water outward from the North Sea.

Plain Language Summary

Seawater temperature simulations are important for researches regarding climate change and for fisheries, protecting coastlines, maintaining the ecological balance, and predicting weather. To improve the seawater temperature prediction capability, a data assimilation (DA) scheme is often applied to combine measurements from observations such as satellites, buoys, and ships with data provided by climate models that consider circulation, wave, atmosphere, and ice components. For decades, various DA methods have been developed with a focus on implementing sophisticated mathematical techniques. However, little attention has been paid to the impacts on physical processes and the secondary effects of DA itself. We used a model and satellite data to investigate the impacts of sea surface temperature (SST) assimilation on the volume and heat budgets over the North Sea. We find that DA, by improving the SST modeling, modifies the budgets of

volume and heat between the North Sea and the Atlantic. The largest change occurs at the Norwegian Channel, where the total water/heat transport from the North Sea outward is reduced. Moreover, SST assimilation also changes the air-sea heat exchange. This study improves our understanding of the relations between model physics and assimilation, which is important for integrating multiple models within a DA framework.

1 Introduction

Regional and coastal studies of ocean temperature have attracted increasing interest from various research communities around the world. This interest is largely driven by concerns related to global warming and the related expected impacts on various densely populated regions. For example, within the period 1983-2012, the sea surface temperature (SST) in the North Sea grew by approximately 0.4°C per decade, with higher increases found in the southern part (Dye et al., 2013). These changes had profound impacts on the biological systems in the North Sea (Kirby et al., 2007) with significant consequences for the economy (e.g., fisheries). Furthermore, regional SSTs have been shown to be of significant importance for the regional weather and climate (Fallmann et al., 2017; Kjellström et al., 2005).

The effects of anthropogenic warming are known to be superimposed with natural variability patterns such as the Atlantic Multi-decadal Oscillation (AMO) (Knight et al., 2005). To better understand the temperature dynamics in, e.g., the North Sea, it is important to consider different components of the coupled system, such as heat fluxes between the atmosphere and the ocean, and the lateral advection of heat across the North West Shelf (Schrum & Backhaus, 1999). However, the exchanges that occur across the shelf edge are complex and still subject of ongoing research (Huthnance et al., 2009). Moreover, because of the strong spatial variations in warming patterns, there is a growing need to further improve the estimation techniques for regional SSTs. One valuable source of information is passive microwave observations obtained from satellites, which provide SST maps on a kilometer scale. There are however limitations regarding the temporal and spatial resolutions of sampling, and passive microwave observations are affected by clouds.

An efficient approach is to assimilate data into numerical models; that is available information about the underlying physics are combined with observations into an optimal estimate. In the pioneering study presented by Annan and Hargreaves (1999), a simpli-

fied Kalman filtering approach was applied to a three-dimensional (3-D) baroclinic model of the North Sea using satellite SST data. By using an anisotropic recursive filter scheme, Liu et al. (2009) assimilated the temperature and salinity profiles in a coastal ocean model, achieving a considerable improvement in the oceanic forecasting efficiency and accuracy. Fu et al. (2011) assimilated the temperature and salinity profiles in a regional ocean model but implemented an ensemble optimal interpolation. Other studies investigated the impacts of the timing and frequency of data assimilation (DA) (Losa et al., 2012) and of the uncertainties of initial states (Losa et al., 2014) on the SST prediction performance. Many of these early studies focused on the predictive skills of models or on the mathematical/statistical aspects of the assimilation technique. Furthermore, standard metrics like root mean square errors (RMSEs) in the prognostic model variables with respect to observations have been used to assess the analysis performance. Hence, the aim of the present study is to analyze the impacts of DA on the water volume and heat budget with a focus on the North Sea. The following questions are at the center of our investigation:

- How does the assimilation of SST observations change the different components of the simulated North Sea heat budget?
- What are the secondary effects of temperature analysis on the remaining prognostic model variables, which are relevant for the heat budget ?
- What can we learn about the North Sea system from the observed responses to applied temperature perturbations?

The exchanges of mass and heat between the North Sea, its adjacent seas, and the atmosphere are complex and influenced by processes on various time scales. The water temperature in the upper ocean is an important component in this system. These lead to the main objective of our study, i.e., to investigate and understand the impact of SST assimilation on physical processes that induce the transports of volume and heat.

In the present study, a 3-D numerical circulation model NEMO (the Nucleus for European Modelling of the Ocean) coupled with the wave model WAM (Staneva et al., 2018) is employed and used for assimilation of OSI SAF (Ocean and Sea Ice Satellite Application Facility) SST satellite measurements (a detailed description is provided in the next section). Wave coupling is important for the temperature evolution of the North Sea because the inclusion of ocean-wave feedback modifies the stresses at the water surface and

improves the simulation of the turbulent mixing layer thickness (Lewis et al., 2019). The DA scheme applied herein is based on the 3-D variation DA (3DVAR) analysis technique, which has frequently been employed in previous ocean studies (Dobricic et al., 2005; Liu et al., 2009). The complete 3-D temperature field is analyzed based on SST observations and assumptions about the vertical and horizontal structures of model errors. The corresponding model error covariance matrix is not constant, but varies over time and space as a function of the mixed layer thickness. Regarding the heat budget of the North Sea, the analysis is performed such that:

- Only the total vertical heat fluxes, including latent and sensible heat fluxes, as well as short and long wave radiation components, between the atmosphere and ocean are considered.
- The lateral advection of heat through open boundaries towards the Atlantic and Baltic Sea is analyzed along transects (see Figure 1), which have already been examined in previous studies (e.g., Hjøllo et al., 2009).
- The tidal and wind-driven components of heat advection as well as those resulting from their interactions are considered separately.

In the assimilation of satellite SST observations, the response of the system to changes in the SST is analyzed such that the consequences of variations in the temperature, surface elevation and current on the heat fluxes are decomposed into separate terms, accounting for different coupling mechanisms. Hence, the lateral advection of heat across the open boundaries of the North Sea is attributed to components related to Eulerian transport, tidal and wind-driven currents, and higher-order nonlinear interactions.

The remainder of this paper is organized as follows: Section 2 includes a description of the coupled NEMO-WAM model, the observational data used and the 3DVAR scheme; furthermore, this section also explains the experimental setup and methods used for analyzing the volume and heat budgets of the North Sea. The modeling results with and without DA are presented in Section 3, followed by Section 4, which further analyzes the model results and compares them with existing studies. The physical processes that induce the advective transport of volume and heat through the open boundaries of the North Sea and the impacts of SST assimilation are discussed in Section 4 as well. The main conclusions are given in Section 5.

2 Data and Methods

2.1 The model system

The Geesthacht Coupled cOAstal model SysTem (GCOAST) is built upon a flexible and comprehensive coupled model system that integrates the most important key components of regional and coastal systems, enabling the inclusion of information from observations (Lewis et al., 2019; Staneva et al., 2019; Ho-Hagemann et al., 2020). GCOAST encompasses: (i) atmosphere-ocean-wave interactions, (ii) the dynamics in and fluxes across the land-sea transition zone, and (iii) the coupling of the marine hydrosphere and biosphere. This model is based on novel numerical modeling concepts, and integrates circulation (NEMO), wave models (WAM), atmosphere model (i.e., the COnsortium for Small-scale Modelling in CLimate Mode, CCLM) and a hydrology model (HD).

The ocean circulation model used in this study is NEMO version 3.6 (Madec & the NEMO team, 2006) with the enhanced implementation of wave physics. The setup covers the region of the Northwest European Shelf, the North Sea, the Danish Straits and the Baltic Sea between $-19.89°$E and $30.16°$E and $40.07°$N and $65.93°$N with a resolution of approximately 3.5 km (Figure 1). The entire model domain is divided into 900 subdomains (approximately 100×100 km in size), with each run in parallel. The vertical grid is the NEMO standard σ-z^* hybrid grid with 50 levels. The model time step adopts the time splitting methodology with a baroclinic time step of 100 seconds. Vertical turbulent viscosities/diffusivities are calculated using the Generic Length Scale (GLS) turbulence model (Umlauf & Burchard, 2003) with the 'k-ϵ' closure scheme and the second-moment algebraic model of Canuto et al. (2001).

The wave model WAM used here is based on the description of wave conditions in the frequency spectrum and in the directional space at each active model grid point within a certain model area. The wave action conservation equation, complemented with a suitable description of the relevant physical processes is used to follow the evolution of each wave spectral component. A detailed description is given by the WAMDI group (The Wamdi Group, 1988; Komen et al., 1994; Günther et al., 1992) and Janssen (2008). WAM Cycle 4.7, which is used for the GCOAST wave hindcasts, is an update of the former WAM Cycle 4. The basic physics and numerical code are kept the same in the new release. The source function integration scheme of Hersbach and Janssen (1999) and the model updates by Bidlot et al. (2007) are incorporated. Similar to the circulation model, the en-

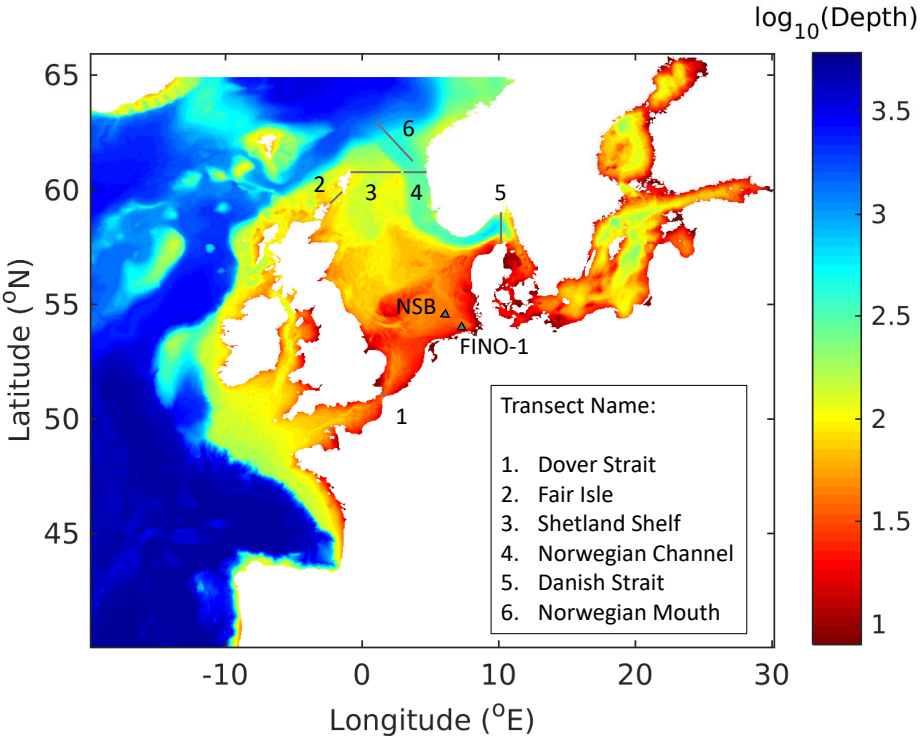

Figure 1. The GCOAST model bathymetry (meters) in a log scale. The location of the transects that used to calculation volume/heat exchange between the North Sea and its adjacent seas are also illustrated. Triangles show the locations of the in-situ observation stations NSB III and FINO-1.

tire model domain is divided into 270 subdomains and run in parallel. The spatial resolution, regional coverage and meteorological forcing are the same as those in NEMO. The model and its performance for the study area are described by Staneva et al. (2016) in more details.

Ocean waves influence circulations through a number of processes: turbulence due to breaking and non-breaking waves, the transfer of momentum from breaking waves to currents in deep and shallow water, wave interactions with planetary and local vorticity, and 1 Langmuir turbulence. The NEMO ocean model has been modified to take into account the following wave effects as described by Staneva et al. (2017, 2019), Alari et al. (2016) and Wu et al. (2019): (1) the Stokes-Coriolis forcing; (2) the sea state-dependent momentum flux; and (3) the sea state-dependent energy flux. Details of the NEMO-WAM model, boundary forcing and parameter settings are further explained in Appendix A.

184 ## 2.2 Observation data

185 ### *2.2.1 Satellite SST data*

186 In this study, the modeled seawater temperature is analyzed with OSI SAF SST data,
187 which are produced by the European Organisation for the Exploitation of Meteorolog-
188 ical Satellites (EUMETSAT). In this study, the North Atlantic Regional (NAR) SST is
189 used, which consists of Metop/Advanced Very High Resolution Radiometer(AVHRR)
190 and Suomi National Polar-orbiting Partnership(SNPP)/Visible Infrared Imaging Radiome-
191 ter Suite(VIIRS) derived subskin SSTs over the North Atlantic and European seas at
192 a 2 km resolution. In the study period (2017), these data are recorded twice a day, i.e.,
193 at 10:00 and 20:00 UTC, with a different number of available points and at different lo-
194 cations due to varying climate conditions (cloud cover). The SST products are compared
195 with Match up Data Bases (MDB) gathered in situ (buoys) measurements and are clas-
196 sified into 6 levels provided at the pixel level: 0: unprocessed, 1: bad/cloudy, 2: worst,
197 3: low, 4: acceptable, 5: excellent. For qualitative use, only values of levels 4 and 5 are
198 employed in this study. More information on OSI SAF products can be found at http://osi-
199 saf.org.

200 ### *2.2.2 Insitu observations*

201 Another important source of information for the present study is fixed measurements from
202 stations in the German Bight operated by the German Federal Maritime and Hydrographic
203 Agency (Bundesamt für Seeschifffahrt und Hydrographie, BSH). Their Marine Environ-
204 mental Monitoring Network in the North Sea and Baltic Sea (MARNET) consists of six
205 automatic oceanographic stations in the North Sea, five of which are currently operat-
206 ing. Most stations measure temperature, salinity, oxygen, sea level, air temperature, wind
207 direction, wind speed and air pressure. In the present study the two MARNET stations
208 Nordseeboje III (NSB III,54°41′ N and 6°47′ E) and FINO-1 (54°00.892′ N and 6°35.258′
209 E)(see Figure 1 for the locations) are used for validation purposes. All data are collected
210 continuously on the platform and are transferred hourly to shore for further processing.

2.3 Assimilation scheme

The assimilation technique used in this study follows the 3DVAR approach which is described in Lorenc (1997). The 3DVAR analysis scheme is based on the minimization of the cost function J defined as

$$J(x) = 0.5(x - x_f)^T B^{-1}(x - x_f) + 0.5(Hx - y)^T G^{-1}(Hx - y) \tag{1}$$

where x_f is the prior state, y is the observation vector, B is the model error covariance matrix, G is the observation error covariance matrix, and H is the observation operator. The critical component of this approach is the definition of matrix B, which determines how the observation information is transferred to model regions, where no observations are available. The most straightforward approach is to prescribe correlation lengths for different dimensions in the model (e.g., horizontal and vertical). This matrix can also be used to consider physical relationships between different model variables to make the analysis dynamically consistent. As is usually the case in the existing literature, matrix G is assumed to be diagonal; i.e., the observation errors are assumed to be spatially uncorrelated. An observation error standard deviation of 0.6 K was used, which is consistent with previous studies (e.g., Grayek et al., 2015). Because of the large state vector dimension, the explicit storage or the inversion of the a priori error covariance matrix B is prohibitively expensive. Therefore, one common approach (Lorenc, 1997) is to define a transformed state $\overline{x}$ as

$$\overline{x} = C^{-1}(x - x_f) \tag{2}$$

with the matrix C, given as

$$(C^{-1})^T C^{-1} = B^{-1} \tag{3}$$

The matrix C^{-1} can be thought of as an operator, that removes correlations, because $\overline{x}$ has a diagonal covariance matrix. With these definitions the cost function J becomes

$$J(x) = 0.5\overline{x}^T\overline{x} + 0.5(HC\overline{x} + Hx_f - y)^T G^{-1}(HC\overline{x} + Hx_f - y) \tag{4}$$

Here, the role of operator C is to add correlations. The gradient of J is given by

$$\nabla J(x) = \overline{x}^T + (HC\overline{x} + Hx_f - y)^T G^{-1} HC \tag{5}$$

or written as a column vector following

$$\nabla J(x)^T = \overline{x} + C^T H^T G^{-1}(HC\overline{x} + Hx_f - y), \tag{6}$$

which can be re-formulated as

$$\nabla J(x)^T = b - Ax \tag{7}$$

with

$$A = -I - C^T H^T G^{-1} HC \ ; \tag{8}$$

$$b = C^T H^T G^{-1}(Hx_f - y) \ . \tag{9}$$

The minimum of the cost function can be found using the condition $\nabla J(x) = 0$, which is solved using a conjugate gradient (CG) method.

The CG method is an iterative technique, which requires multiple applications of the matrix A (eq. 8) to given state vectors. Because of the high state dimension, these operations are computationally demanding. The 3DVAR implementation of the Geesthacht Assimilation System (GALATON3DVAR) applied in this study is therefore making use of the parallelized implementation of the circulation model. The filter operations are distributed over different processes assigned to the various model subdomains. The required information exchange between subdomains is implemented using the Message Passing Interface (MPI). GALATON3DVAR uses pre-computed index tables and is applicable for both regular and irregular model grids.

In the standard 3DVAR scheme, the error covariance matrix B is constant over time. In this study we make the vertical error correlation length, which is included in the formulation of B, dependent on the mixing layer thickness. This approach is based on the

assumption that the mixed layer thickness of the free model is within a reasonable error margin. In that case, by definition, the complete mixed layer temperature will be affected by the same error as the SST. Thus, the vertical model error correlation length varies both in time and space with the evolution of turbulent mixing.

Furthermore, the horizontal correlation length of model errors required for the formulation of matrix B is assumed to be constant over both time and space with a value of 5 km. This value represents a compromise between retaining small-scale structures introduced by the satellite measurements into the system and simultaneously extrapolating observations to fill data gaps.

It is important to emphasize that the mixed layer thickness is significantly dependent on ocean waves, which impact both the air/sea momentum fluxes and the turbulent kinetic energy in the upper ocean layers. For this reason the coupling of the circulation model and the ocean wave model is an important factor in the applied DA method.

2.4 Experimental setup

To initiate the DA with a relatively balanced state, a spin-up run of more than 3 years (from 15 October, 2013 to 1 January, 2017) is performed with the coupled GCOAST system. Beginning on 1 January 2017, the model is run without DA for one year; this run is denoted as the "Free Run" case. Then, the model is restarted from 1 January 2017 with the same settings, but the OSI SAF SST data are assimilated; this run is denoted as the "DA Run". In the DA Run, only the satellite data at 10:00 each day are used for the analysis according to the 24-hour assimilation interval.

Note that the circulation model NEMO is also run without being coupled to the wave model WAM, and the same OSI SAF SST data set is applied for the assimilation. This configuration is used only for a comparison with the coupled model run to inspect the impact of coupling on the SST simulation. Hence, in the following sections, the DA Run refers to the coupled assimilation run unless otherwise specified as being "uncoupled".

To determine the water and heat exchanges between the North Sea and the adjacent seas, five transects are selected through the eastern (Dover Strait), northern (Fair Isle, Shetland Shelf, and Norwegian Channel) and western (Danish Strait) open boundaries of the

North Sea (Figure. 1); these transects are equivalent to sections N13, N3, N1 N2 and N22, respectively, of the North West European Shelf Operational Oceanographic System (NOOS) (NOOS, 2010). The transports of volume and heat across these transects are computed at 3 hour and 6 hour intervals, respectiely.

2.5 Volume and heat transports

To analyze the volume budget for the North Sea, the water transport through the five transects illustrated in Figure 1 is considered. The water transport is computed as

$$q^{\mathrm{V}} = \int_A u \, \mathrm{d}A, \tag{10}$$

where A is the area of the 2D transect plane and u is the current component perpendicular to the plane. Regarding the heat budget, both lateral heat transport and air-sea heat exchange should be considered; the former is due to the transport of water with different temperatures, while the latter consists of four main processes: heat fluxes due to shortwave and longwave radiation, and latent and sensible heat fluxes. Note that the present study focuses on the total heat budget over the North Sea and thus does not distinguish individual processes in the atmosphere-ocean heat flux exchange. The advective heat transport is given by

$$q^{\mathrm{H}} = \int_A u \, c_p \, \rho \, T_K \, \mathrm{d}A, \tag{11}$$

and the incremental area is expressed as $\mathrm{d}A = \mathrm{d}h \;\; \mathrm{d}z$, where $\mathrm{d}h$ and $\mathrm{d}z$ are the grid sizes in the horizontal and vertical directions, respectively. Note that due to the $\sigma - z^*$ hybrid grid used in the model, $\mathrm{d}z$ depends on the water elevation and local depth. The constant $c_p = 4.19 \times 10^3$ $\mathrm{J^{-1}kg^{-1}K^{-1}}$ is the heat capacity constant, $\rho = 1026$ kg $\mathrm{m^{-3}}$ is the reference seawater density, and T_K is the temperature in K. Note that positive flux values refer to mass and heat flow into the North Sea; i.e., positive is northeastward along the transect Dover Strait transect, southeastward along the Fair Isle transect, southward along the Shetland Shelf, and Norwegian Channel transects, and westward at the Danish Strait transect. Hence, summing all the positive and negative transports of grid cells separately over the study period yields inflow and outflow through each transect. Then, the net transport is obtained by adding up the total inflow and outflow. This approach

is adopted to avoid large numerical rounding errors that may occur in a straightforward sequential summation of position and negative numbers.

Since heat transport is affected by changes in the water level, current speed and temperature, all these effects and their coupling will be analyzed in the following. First, the velocity normal to the transect, the water layer thickness and the temperature in the DA Run are written as $u_\mathrm{a} = u_f + u_\mathrm{d}$, $\mathrm{d}A_\mathrm{a} = \mathrm{d}A_\mathrm{f} + \mathrm{d}A_\mathrm{d}$, and $T_\mathrm{a} = T_\mathrm{f} + T_\mathrm{d}$, respectively, with the subscript d denoting the differences in variables between the Free Run (f) and DA Run (a). Moreover, $T_K = T - T_r$ (where T is the temperature in°C and $T_r = 6$ °C the reference temperature) (Dieterich et al., 2019). Thus, eq. 10 is decomposed for the DA Run as

$$q_\mathrm{a}^\mathrm{V} = \underbrace{\int_{A_\mathrm{f}} u_\mathrm{f}\,\mathrm{d}A_\mathrm{f}}_{\mathrm{V}_1} + \underbrace{\int_{A_\mathrm{f}} u_\mathrm{d}\,\mathrm{d}A_\mathrm{f}}_{\mathrm{V}_2} + \underbrace{\int_{A_\mathrm{d}} u_\mathrm{f}\,\mathrm{d}A_\mathrm{d}}_{\mathrm{V}_3} + \underbrace{\int_{A_\mathrm{d}} u_\mathrm{d}\,\mathrm{d}A_\mathrm{d}}_{\mathrm{V}_4}, \tag{12}$$

and the heat transport (eq. 11) as

$$\begin{aligned} q_\mathrm{a}^\mathrm{H} \quad = c_p\,\rho\,[\quad & \underbrace{\int_{A_\mathrm{f}} u_\mathrm{f}\,T_\mathrm{f}\,\mathrm{d}A_\mathrm{f}}_{\mathrm{P}_1} + \underbrace{\int_{A_\mathrm{f}} u_\mathrm{f}\,T_\mathrm{d}\,\mathrm{d}A_\mathrm{f}}_{\mathrm{P}_2} + \underbrace{\int_{A_\mathrm{f}} u_\mathrm{f}\,(-T_\mathrm{r})\,\mathrm{d}A_\mathrm{f}}_{\mathrm{P}_3} + \underbrace{\int_{A_\mathrm{f}} u_\mathrm{d}\,T_\mathrm{f}\,\mathrm{d}A_\mathrm{f}}_{\mathrm{P}_4} + \\ & \underbrace{\int_{A_\mathrm{f}} u_\mathrm{d}\,T_\mathrm{d}\,\mathrm{d}A_\mathrm{f}}_{\mathrm{P}_5} + \underbrace{\int_{A_\mathrm{f}} u_\mathrm{d}\,(-T_\mathrm{r})\,\mathrm{d}A_\mathrm{f}}_{\mathrm{P}_6} + \underbrace{\int_{A_\mathrm{d}} u_\mathrm{d}\,T_\mathrm{f}\,\mathrm{d}A_\mathrm{d}}_{\mathrm{P}_7} + \underbrace{\int_{A_\mathrm{d}} u_\mathrm{f}\,T_\mathrm{d}\,\mathrm{d}A_\mathrm{d}}_{\mathrm{P}_8} + \\ & \underbrace{\int_{A_\mathrm{d}} u_\mathrm{f}\,(-T_\mathrm{r})\,\mathrm{d}A_\mathrm{d}}_{\mathrm{P}_9} + \underbrace{\int_{A_\mathrm{d}} u_\mathrm{d}\,T_\mathrm{f}\,\mathrm{d}A_\mathrm{d}}_{\mathrm{P}_{10}} + \underbrace{\int_{A_\mathrm{d}} u_\mathrm{d}\,T_\mathrm{d}\,\mathrm{d}A_\mathrm{d}}_{\mathrm{P}_{11}} + \underbrace{\int_{A_\mathrm{d}} u_\mathrm{d}\,(-T_\mathrm{r})\,\mathrm{d}A_\mathrm{d}}_{\mathrm{P}_{12}}\,]\,. \end{aligned} \tag{13}$$

In eq. 12, V_1 is the Free Run volume transport, V_2 is the volume transport due to the modification of the velocity, V_3 is the volume transport due to the modification of the sea surface height, and V_4 is associated with the nonlinear interaction between the improved velocity and sea surface height. In eq. 13, P_1 and P_3 are the heat transports of the Free Run, P_2 denotes the heat transport due to the temperature change by DA, P_4 and P_6 are the heat transports due to the velocity change by DA, and P_7 and P_9 are the heat transports due to the sea surface height changes by DA. The terms P_5, P_8, P_{10} through P_{12} are the transports due to nonlinear couplings between the velocity, sea surface height and temperature changes resulting from DA.

3 Results

3.1 Improved agreement of the modeled seawater temperature

To assess the DA performance in the study period, Figure 2 shows SST of the OSI SAF and of the model runs on 1 July and 31 December 2017. These days are in the middle and at the end of the assimilation period, respectively. Although the OSI SAF data availability varies in both space and time (see Figure 2a and Figure 2e), the updates of the model introduced by DA can by kept and accumulated over time. Obvious differences between the OSI SAF data and the model data are visible in the Atlantic Ocean, where the OSI SAF SST is higher than that in the Free Run. In the North Atlantic, especially above 60°N, the SST in the Free Run is underestimated by approximately 2.5°C to 3.5°C. In the North Sea, the SST is increased by 0.5°C to 1°C due to DA (Figure 2h). In the Baltic Sea, the Free Run SST is lower than the DA Run SST in July (Figure 2d), while the former is higher in December (Figure 2h). Furthermore, it is worth to noting that the large spatial scale SST features in the Free Run (Figure 2b and f) are kept in the DA Run (Figure 2c and g); moreover, smaller-scale features are introduced by the analysis (e.g., comparing the SST structures in Figure 2f and g at 60 to 62°N, -5 to 5°E on 31 December). Note that the OSI SAF SST is shown at 10:00 while the model data are shown at 12:00. The temperature difference in two hours is negligible since the daily seawater temperature cycle is small compared with the SST variation due to analysis.

The numbers of available OSI SAF data points for the model grid used for DA over the full model domain are plotted in Figure 3. Due to cloud cover, the number of valid observation data points roughly varies from 1 $\times 10^4$ to 7 $\times 10^4$. In general, the number of valid observations is smaller in wintertime (November to April) than in summertime (May to October). Figure 3 also compares the temporal evolution of RMSEs of the model with and without DA, showing that the Free Run has an RMSE of 0.7°C $\sim$ 1.8°C, whereas after DA, the RMSE is reduced to 0.3°C $\sim$ 0.9°C. Furthermore, the DA scheme is able to keep the analyzed SST close to the observations even when the Free Run shows strong departures. For example, in the early stage of the study period (February to May), the RMSE difference between the Free Run and DA Run is approximately 0.2°C $\sim$ 0.3°C, while at the end of 2017 (October to December), the RMSE becomes 0.5°C $\sim$ 0.6°C. Compared with the uncoupled DA Run, the coupling improves the SST simulation in the periods when the North Sea is both warming up and cooling down. From June to August,

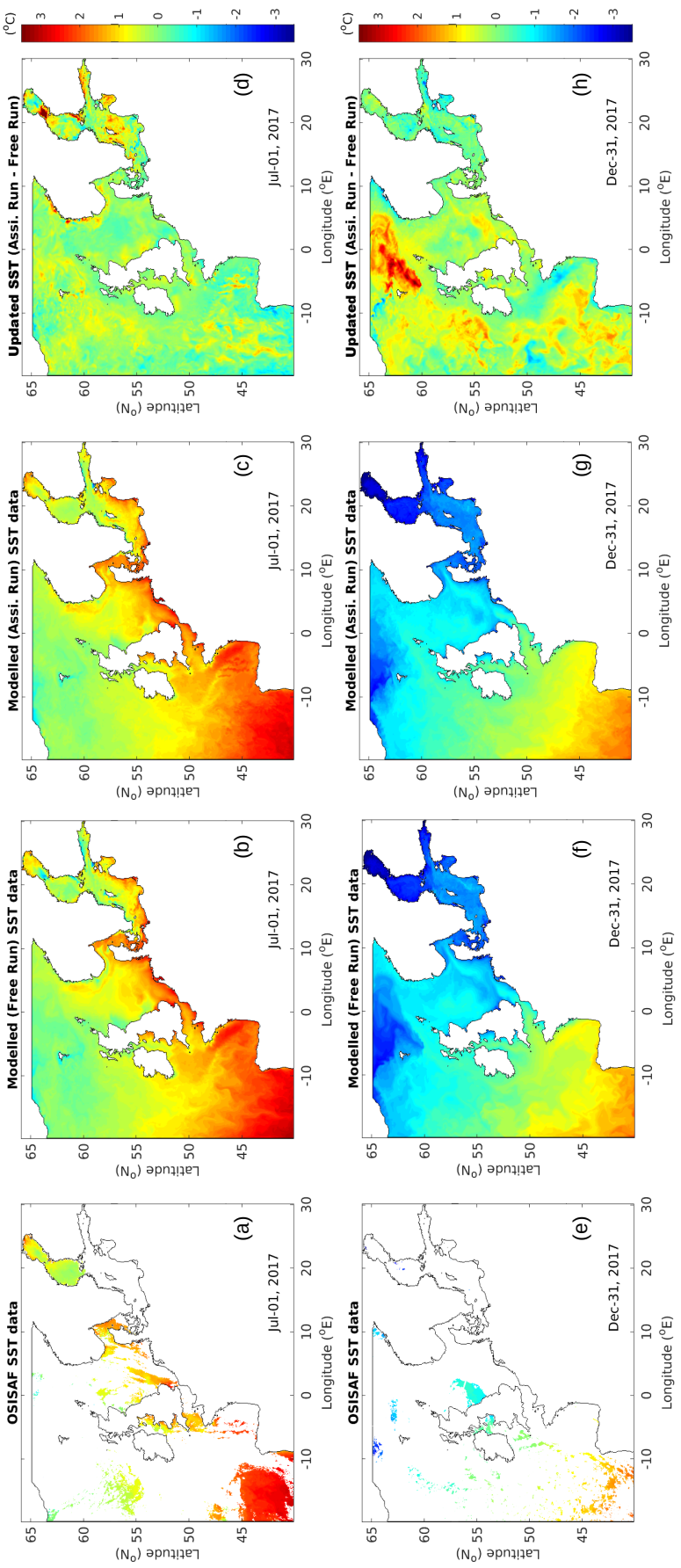

Figure 2. SST in °C from (left column) OSI SAF data, (middle column) model without assimilation (Free Run), model with assimilation (DA Run) and model update of the assimilation (DA Run - Free Run), respectively. Upper panels show data in the middle of the analyzed period (1 July 2017) and lower panels refer to the end of the analyzed period (31 December 2017).

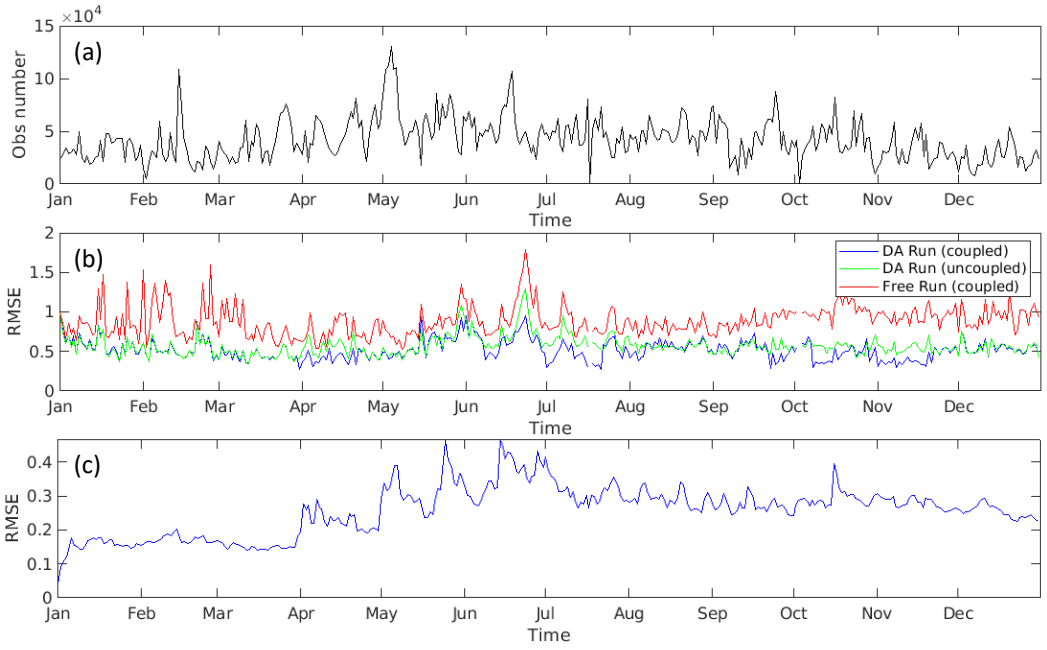

Figure 3. Time evolution of (a) the number of OSI SAF SST, (b) the root mean square error (RMSE,°C) between the OSI SAF SST and the DA Run SST with and without coupling, and the Free Run SST; (c) is the RMSE between the coupled DA Run SST and the uncoupled DA Run SST over 2017.

wave coupling reduces the RMSE by 0.3°C while in October and November, the RMSE reduces by approximately 0.2°C. Further comparison between the coupled and uncoupled DA Run results reveals RMSEs of 0.2 to 0.3°C over the North Sea.

Figure 4 compares the modeled (coupled DA) temporal variation of the temperature with that of the independent MARNET data acquired at NSB III and FINO-1 (see Figure 1 for their locations) at different water depths. The OSI SAF SST data over the study period are plotted at these two locations together with the near-surface temperature data at a depth of 3 m. Note that the OSI SAF SST is unavailable when the station is covered by clouds or the data quality is low. The comparison at this water layer verifies the consistency between the OSI SAF data and the in-situ data. At NSB III station (Figure 4a-c), the Free Run has already shown a good capability to simulate the temperature evolution in 2017 despite an underestimation of approximately 1°C to 2°C in the middle water layers between June and July (Figure 4d). The DA Run provides slightly better results than the Free Run. At FINO-1, the DA leads to obvious improvements in the performance of seawater temperature simulation (Figure 4e-g). Especially in the first

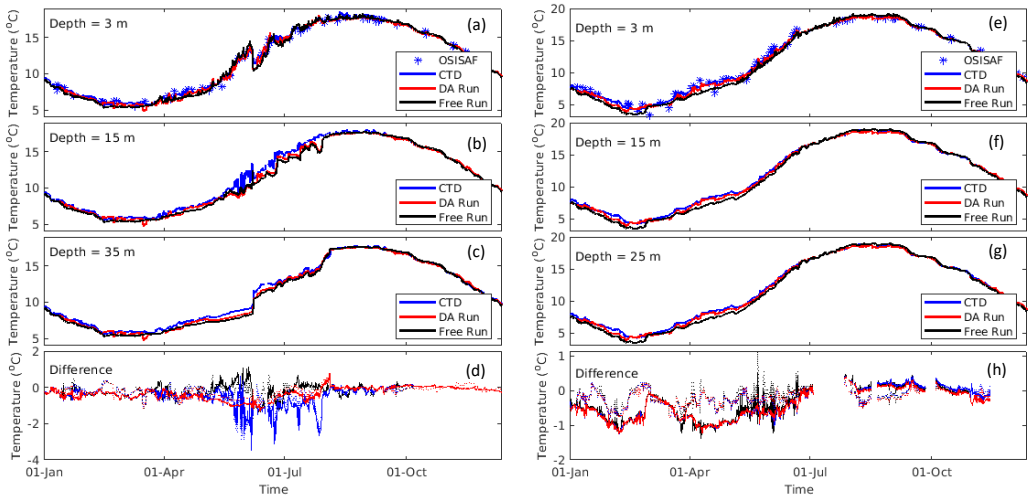

Figure 4. Time evolution of the temperature at the MARNET station "NSB-III" (left) and "FINO 1" (right) for (a, e) near the surface, (b, f) the middle water depth and (c, g) near the bottom, respectively. Panels (d) and (h) show the temperature difference between the Free Run and the CTD measurements (solid lines), the DA Run and the CTD measurements (dotted lines) near the surface (black), the middle depth (blue) and the bottom (red).

half of the study year (January to July), the underestimated temperature (approximately 1°C) between the Free Run and the MARNET data is corrected in the DA Run. Due to the relatively shallow water depth and mixing of the water column, the DA Run also shows representative temperature evolution near the sea bed ((Figure 4h).

3.2 Volume budget

The volume transport through each of the five selected transects in the North Sea (see Figure 1) is computed over the study period (see eq. 10) and illustrated in Figure 5a. The transects are selected following previous studies (NOOS, 2010). Net transport into the North Sea is observed through the Dover Strait, Fair Isle and Shetland Shelf, while net outward transport occurs through the Norwegian Channel and Danish Strait. In the Free Run, the net transport through the Dover Strait (approximately 0.088 Sv, 1 Sv ≡

384 10^6 m^3s^{-1}) is the smallest among the three inward transects, accounting for 7.1 % of the
385 total inward volume transport. In contrast, at Fair Isle and Shetland Shelf, the net trans-
386 port is 0.54 Sv and 0.61 Sv, respectively, accounting for 43.8 % and 49.1 % of the net
387 water transport into the North Sea. Regarding the outward volume transport, 0.82 Sv
388 exits through the Norwegian Channel (61.1 %), and 0.52 Sv exits through the Danish
389 Strait (38.9 %). In the DA Run, the inward volume transports are 0.08 Sv (6.9 %) through
390 the Dover Strait, 0.49 Sv (42.5 %) at Fair Isle and 0.59 Sv (51 %) along the Shetland
391 Shelf, while the outward transports are 0.68 Sv (57 %) through the Norwegian Chan-
392 nel and 0.51 Sv (43 %) through the Danish Strait. Note that in the Free Run, the to-
393 tal volume transport into the North Sea (1.24 Sv) is approximately 92.5 % of the total
394 volume loss (1.34 Sv). With DA, the model shows a decrease in both the inward and the
395 outward volume transports and exhibits a better match between them. In the DA Run,
396 the total inward volume transport is 1.16 Sv, which accounts for 97 % of the total out-
397 ward transport (1.19 Sv). Compared with the volume exchange between the North Sea
398 and the Atlantic, river runoff is negligible. The total river discharge into the North Sea
399 is approximately 300 cubic km/year (Quante & Colijn, 2016), which is only approximately
400 0.01 Sv. The modeled volume budget (as well as the heat budget presented in the next
401 section) in the present work are further compared with those of existing studies in Sec-
402 tion 4.

403 Figure 5b compares the volume transport composition of the DA Run along each
404 transect, demonstrating that the differences between the Free Run volume transports
405 represented by the term V_1 in eq. 12 and the analyzed transport are mainly due to the
406 term V_2, which is associated with changes in the current field, whereas the contributions
407 of V_3 and V_4 are negligible. Interestingly, the sign of V_2 is opposite to that of V_1 on all
408 transects, which implies that DA always tends to decrease the net volume transport. It
409 is worth noting that through the Norwegian Channel V_2 is significant, accounting for nearly
410 20 % of the total transport along this transect; this implies a strong impact of the SST
411 assimilation on the velocity fields. The potential physical processes responsible for this
412 are further explored and discussed in Section 4.

413 ### 3.3 Heat budget

414 Neglecting the small heat flux associated with river runoff, the heat content in the North
415 Sea depends mainly on two processes: lateral heat transport through the open bound-

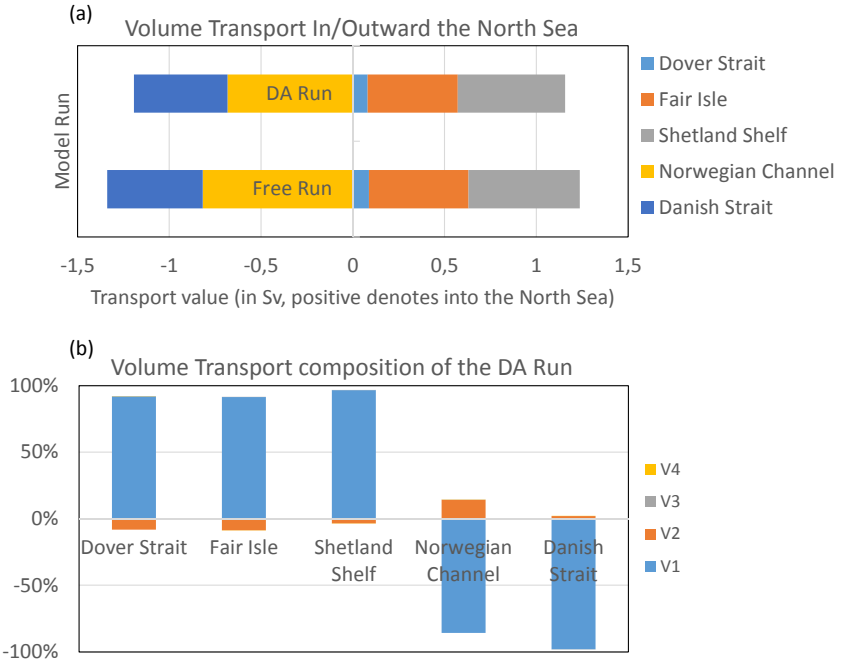

Figure 5. (a) The annual mean volume transports (in Sv) through the selected transects; (b) Volume transport composition of the DA Run (positive/negative denotes into/out the North Sea).

aries (the five selected transects illustrated in Figure 1) and heat exchange between the air and sea at the water surface. Figure 6a shows the heat transport through each of the selected transects. Since the advective heat transport is largely determined by the volume transport, the heat transport distribution through the open boundaries of the North Sea is similar to the volume transport distribution; i.e., the North Sea gains heat through the Dover Strait, Fair Isle and the Shetland Shelf, loses heat through the Norwegian Channel and the Danish Strait. However, due to differences in the local temperature features of seawater, the heat transport ratios through these transects are different from the volume transport ratios. Despite the low volume transport through the Dover Strait, the high seawater temperature results in a large amount of heat into the North Sea (2.74 TW, which accounts for 13 % of the total transport in the Free Run, and 2.69 TW in the DA Run, i.e., 13 %). Likewise, through the Danish Strait, the amount of heat lost in the Free Run (DA Run) is 7.21 TW (7.51 TW), which accounts for 41.3 % (44.3 %) of the total loss. In total, the North Sea gains 21 TW (20.78 TW) of heat and loses 17.77 TW (16.05 TW) in the Free Run (DA Run), with a net of 3.23 TW (4.74 TW). This yields net heat gain/heat loss ratios of 118 % and 130 % for the Free Run and DA Run, respectively.

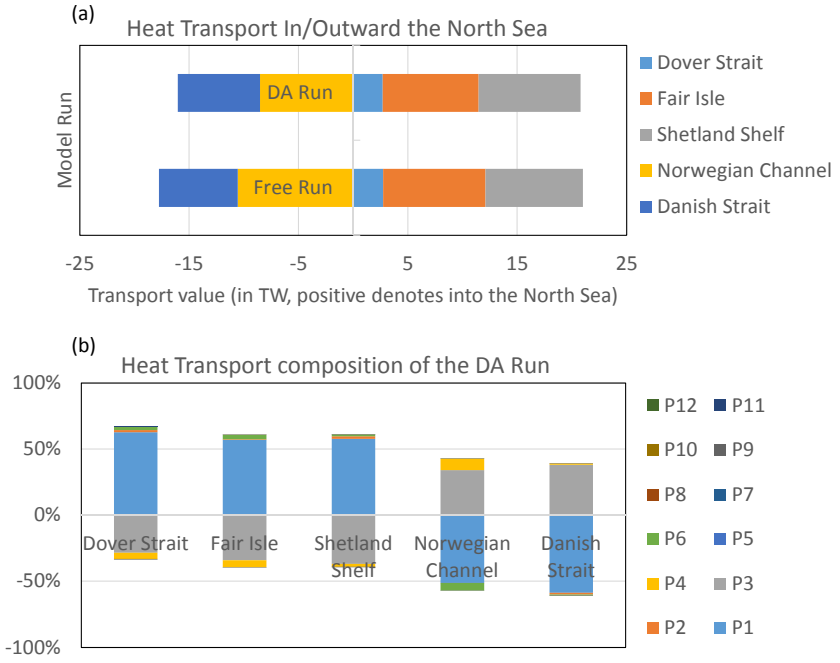

Figure 6. (a) The annual mean heat transports (in TW) through the selected transects; (b) Heat transport composition of the DA Run (positive/negative denotes into/out the North Sea).

In other words, with DA, more heat enters the North Sea via lateral advection, during the considered period.

Further computing the heat transport composition in the DA Run (Figure 6b) reveals that the main difference between the DA Run and Free Run is due to the transport of water at the reference temperature (i.e., P_3). The choice of a reference temperature and its impacts on the relative values of heat fluxes are further discussed in the next section. Other terms that contribute to the DA improvement in heat transport are P_4 and P_6, especially at the Norwegian Channel. These two terms are both caused by the improvement in volume transport due to DA, which, as discussed in the previous section, is correlated with the changes in hydrodynamics.

With regard to air-sea heat exchanges, Figure 7 shows the annual mean heat fluxes over the North Sea. Evidently, the assimilation of SST data does not change the spatial pattern of air-sea heat fluxes. In both the Free Run (Figure 7a) and the DA Run (Figure 7b), the North Sea gains heat from the atmosphere in the middle of the domain close to the British coast and loses heat along the northern and southern boundaries. The Free Run yields a net heat gain for the central North Sea with a maximum value of 30 W m^{-2} and

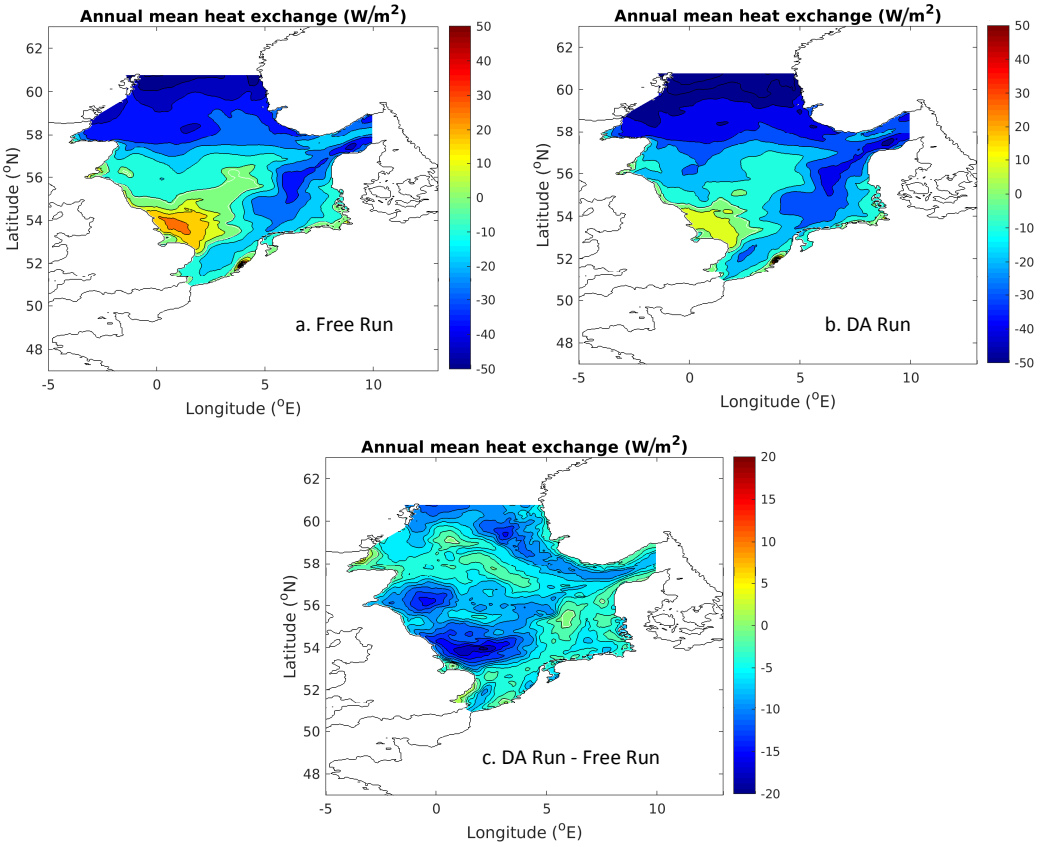

Figure 7. The annual mean heat fluxes (in W m^{-2}) between the atmosphere and the sea (a) the Free Run, (b) the DA Run and (c) the air-sea heat exchange updated caused by the DA. In (a) and (b), positive/negative values denote fluxes inward/outward the ocean.

a net heat loss for the area close to the northern boundary with a minimum value of -50 W m^{-2}. In the DA Run, the maximum net heat gain is approximately 10 W m^{-2} while the maximum net heat loss is approximately -60 W m^{-2}. As shown in Figure 7c, the assimialtion of SST data results mainly in a reduction in the heat gain from the atmosphere in the middle of the North Sea and the Norwegian Channel. For the entire North Sea domain, the total annual mean air-sea heat flux is reduced from -7.97 TW to -11.08 TW (i.e., a constant heat flux change of -5 W m^{-2}).

Figure 8 shows the annual accumulation of net heat transport over the North Sea. The heat transport between the air and sea exhibits a strong strong seasonal cycle (approximately 3.5×10^{20} J) with warming of the North Sea from April to October and cooling during the remainder of the period. This negative heat transport suggests a net heat

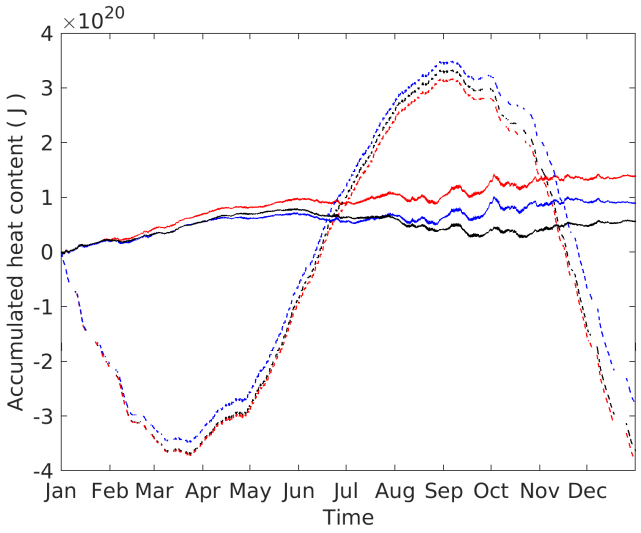

Figure 8. Temporal accumulation of the net heat transport (in J) into the North Sea in 2017. Solid lines are net advective heat transports and dashed lines denote heat transports from the atmosphere to the North Sea. Positive/negative is the net heat transport towards/outwards the North Sea. Black curves denote the uncoupled DA run, blue and red curves correspond to the coupled Free and DA Run, respectively.

loss for 2017 in the North Sea due to air-sea heat exchange. Advective heat transport shows a continuous heat gain trend from the North Atlantic Ocean to the North Sea. In the Free Run, the North Sea looses approximately 2.6 $\times$ 10^{20} J via the air-sea interface, while it gains 0.8 $\times$ 10^{20} J from lateral water transport. In the DA Run, the North Sea looses approximately 3.7 $\times$ 10^{20} J via the air-sea interface and gains 1.3 $\times$ 10^{20} J from lateral water transport. In other words, both heat transport processes are enhanced by DA, albeit with a different sign. This indicates that the North Sea gains more heat through lateral advection (0.5 $\times$ 10^{20} J) and loses extra heat due to air-sea heat exchange (0.9 $\times$ 10^{20} J). On the one hand, the net heat gain by lateral advection warms the North Sea, while on the other hand, the increase in the ST by assimilation also enhances the heat flux from the sea to the atmosphere. Comparing the two model runs, the net heat loss due to air-sea heat exchange compensated by advective transport is increased from 30 % to 35%. It is worth noting that wave coupling also enhances the net heat gain in the North Sea via advective transport (by modifying the momentum budget at the ocean surface (Lewis et al., 2019)), whereas the impacts of coupling on air-sea heat exchange are minor.

4 Discussion

4.1 Transport estimates

To assess the transports computed in the current study, earlier investigations are reviewed regarding the average rates of volume and heat exchanges between the North Sea and its adjacent seas. The net inflow through the Dover Strait to the North Sea computed by the model, approximately $0.080 \sim 0.088$ Sv, which is close to the field measurements (0.09 Sv) reported by Prandle et al. (1996), who estimated these values based on high-frequency (HF) radar and bottom-mounted acoustic Doppler current profiler (ADCP) profiles spanning 1 year. At Fair Isle, the net inflow of 0.54 Sv in the Free Run (0.49 Sv in the DA Run) is higher than the observations (0.36 Sv) reported by Otto et al. (1990) but close to the value of 0.49 Sv obtained by taking the annual mean of a model study (Winther & Johannessen, 2006). A consistent value is also found for the Shetland Shelf, where the observed net inflow is approximately 0.6 Sv (Otto et al., 1990). At the Norwegian Channel, Otto et al. (1990) observed an inflow flux of approximately 0.7 Sv to 1.1 Sv and an outflow flux of 1.8 Sv, yielding a net outward flux of $0.7 \sim 1.1$ Sv from the North Sea. Based on the model study of Winther and Johannessen (2006), Hjøllo et al. (2009) computed the annual mean volume transport through the Norwegian Channel, arriving at 1.23 Sv (2.33 Sv) into (out of) the North Sea. Hjøllo et al. (2009) further calculated the mean monthly inflow/outflow between 1985 and 2007, resulting in values of 1.02 Sv/1.98 Sv, which yields a similar net outflow of 0.96 Sv that falls within the range of observations. Note that these values are slightly larger than the values derived in our study (0.82 Sv/ 0.68 Sv for the Free Run/DA Run) mainly because the Norwegian Channel transect we used is longer than the transects of earlier studies and thus includes the southward along-shelf current from the Atlantic on its western side. Along the eastern open boundary, there are two main water masses: the inflowing North Sea Norwegian Coast Current (NCC) and the outflowing North Sea Jutland Current (JC). On average, these two currents are roughly balanced in exchanges (Danielssen et al., 1997; Winther & Johannessen, 2006; Hjøllo et al., 2009). In the current study, the Danish Strait transect is located north of Skagen, Danmark. The net inflow of the NNC is small and hence yields a net outflow volume transport of approximately 0.5 Sv.

The choice of reference temperature will not only directly affect the magnitude of heat transport (see eq. 13, P3) but also indirectly influence the amount of DA-induced change

in heat transport (see eq. 13, P6, P9, and P12). In the following, different reference temperatures (T_{ref}) are used in eq. 13, which enables us to conduct an analysis of the sensitivity of advective heat transport to the heat budget. Figure 9a shows the net heat transport through different transects for $T_{\mathrm{ref}} = 0°\mathrm{C}$. The net heat transport through each transect is much larger than that in the $T_{\mathrm{ref}} = 6°\mathrm{C}$ case (see Figure 6a), which was also applied by Dieterich et al. (2019). This is because, when T_{ref} is greater than 0 °C, the transport term, P1, is reduced by P3. In this case, the total advective heat transport is 0.6 TW in the Free Run (3.79 TW in the DA Run). Since the advective heat transport into the North Sea exhibits a strong annual variation (Hjøllo et al., 2009), it is difficult to compare the exact values of the present work with those of early studies. However, the magnitude is rather close. For example, Hjøllo et al. (2009), who also used $T_{\mathrm{ref}} = 0°\mathrm{C}$, computed the heat transport through the western boundary (0°E, $49 \sim 50.5$°N), the northern boundary (2°W ~ 5°E, 59.2°N), and the eastern boundary ($8.1 \sim 8.6$°E, $57.1 \sim 58.1$°N), and the results show that the monthly mean net transport in 1985∼2007 through these boundaries varied between 0 and 10 TW, -15 and 8 TW, and -5 and 8 TW, respectively. The total North Sea advective inflow heat reached a mean of 2.6 TW during this period. Our sensitivity study shows that the net advective heat transport in the North Sea increases linearly with increasing T_{ref} (Figure 9b). Clearly, after implementing DA, the net transport becomes much insensitive to the choice of T_{ref} and reaches a value of 4.7 ± 0.5 TW. This is because the sensitivity of heat transport to the reference temperature grows with an increasing current speed (see 13, P6). As the currents are reduced by the analysis on average, especially at the Norwegian Channel (Figure 5b), the DA is less sensitive to T_{ref}.

Figure 8 shows that the lowest heat content due to air-sea heat exchange occurs in late March, while the highestheat content exists in early September for both the Free Run and the DA Run. This finding implies that the DA mainly changes the amplitude of air-sea heat exchange while hardly having an effect on the temporal evolution pattern itself. For both the Free Run and the DA Run, the seasonal variation of the air-sea heat exchange is approximately 6.5×10^{20} J (the difference between the net heat transport maximum in September and the minimum in late March). This is consistent with the 20-year model study result of Hjøllo et al. (2009), who defined the seasonal variation of the air-to-sea heat transport as a heat gain of $5 \sim 6 \times 10^{20}$ J.

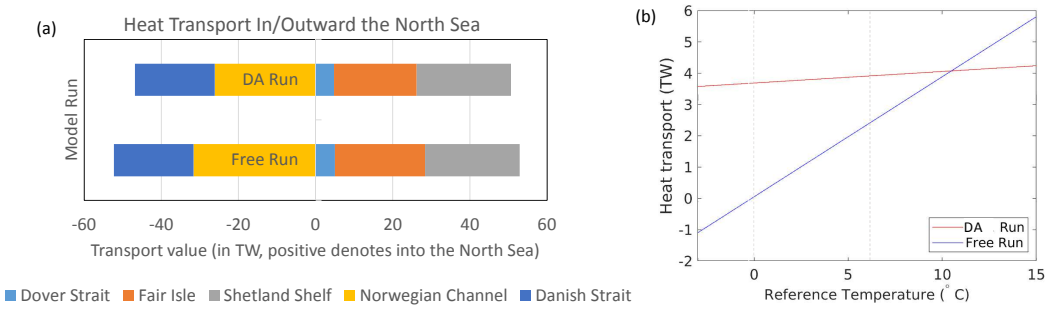

Figure 9. (a) Similar as Figure 6(a) but for $T_{\mathrm{ref}} = 0°\mathrm{C}$; (b) Net heat transport into/out of the North Sea by lateral advection as a function of varying T_{ref}. Positive/negative values denote gain/loss heat of the North Sea. Vertical dashed lines indicate $T_{\mathrm{ref}} = 0°\mathrm{C}$ and $T_{\mathrm{ref}} = 6°\mathrm{C}$.

4.2 Mixing layer thickness

As explained in Section 2.3, the thickness of the mixing layer determines the depth to which the correction of the SST caused by DA will reach. Hence, a well-resolved mixing layer depth is necessary to eliminate systematic errors in ocean temperature simulations. Earlier studies have identified the need for wave coupling to improve the performance for the annual variation of the mixing layer depth, in which the impact of coupling on temperatures could be diminished by DA (Lewis et al., 2019). This also motivates the implementation of the coupled NEMO-WAM model in the present study. Nevertheless, the circulation-wave interaction is rather more complex than simply a weakening or enhancing of the mixing layer depth at a certain time or location. The focus of this study is, however, on the DA related aspects of estimating the heat budget, and thus, we will perform a more detailed analysis of the coupling mechanisms in a separate follow-up investigation.

Figure. 4 shows that at NSB-III, the SST DA successfully corrects the water temperatures in the middle water layers. However, DA hardly improves the temperatures in the deep water from May to July. This is consistent with the annual variation of the mixing layer thickness, which is only 10 m during this period and reaches the bottom during the remainder of the year (not shown). Under well-mixed conditions, for example at FINO-1, along the Dover Strait and Fair Isle transects, the assimilation of SST data can improve the temperature over the entire water column.

To further discuss the behavior of the mixing layer depth and the associated temperature profile corrections in partially stratified water columns, Figure 10 illustrates the annual variation of the seawater temperature, including Free/DA Run difference, and mixing layer thickness at the Shetland Shelf and Norwegian Channel. At these two locations, the water column is stratified in the summertime and becomes increasingly mixed as the water temperature in the upper layer cools. The thickness of the temperature correction agrees well with the mixing layer depth distribution. Moreover, the water layer "memorizes" the corrections of the prior state. Such a memory could last for months if the hydrodynamic conditions are sufficiently stable. For example, at the Shetland Shelf (Figure 10b), in early May the temperature correction reaches 100 m above the bottom, which is consistent with the mixing layer thickness. From late May until September, the stratification is rather stable, and the mixing layer thickness remains only 25 m. Within this layer, the water temperature is reduced (-0.5°C) due to the DA, whereas in the layers below down to 100 m above the bottom, the temperature corrections (approximately $+0.5$°C) performed in early May are still visible.

The DA also cools the surface temperature at the Norwegian Channel (within the top 25 m between June and late August). However, at water depths below the mixing layer depth, the temperature is corrected in the opposite direction. From late July to early August, the temperature of the water column $40 \sim 60$ is increased by 1.5°C, whereas prior to this period the difference between the Free Run and the DA Run is small (less than 0.1°C). Similar features are observed in October: warming ($+1.5$°C) of the water column inside the mixing layer coupled with a cooling (-1.5°C) below. These changes below the mixing layer are not caused by the DA directly but are rather related to the response of the system to the updated state vector. The main effect here is a lateral advection of nonlocal water mass from the side in the deep layers. These water bodies are originate from two sources. One is the southward current from the Atlantic that enters the North Sea along the western shelf edge of the Norwegian Channel, especially near the bottom; the second is the northward NCC in the middle and eastern parts of the Norwegian Channel. Holt and Proctor (2008) demonstrated that these two currents interact, forming eddies with many small scale features. These features are sensitive to changes in density, since they perturb the local geostrophic balance and hence the current profile by DA. Variations in the density field change the pressure gradient in the horizontal direction and also impact the stability of the water column.

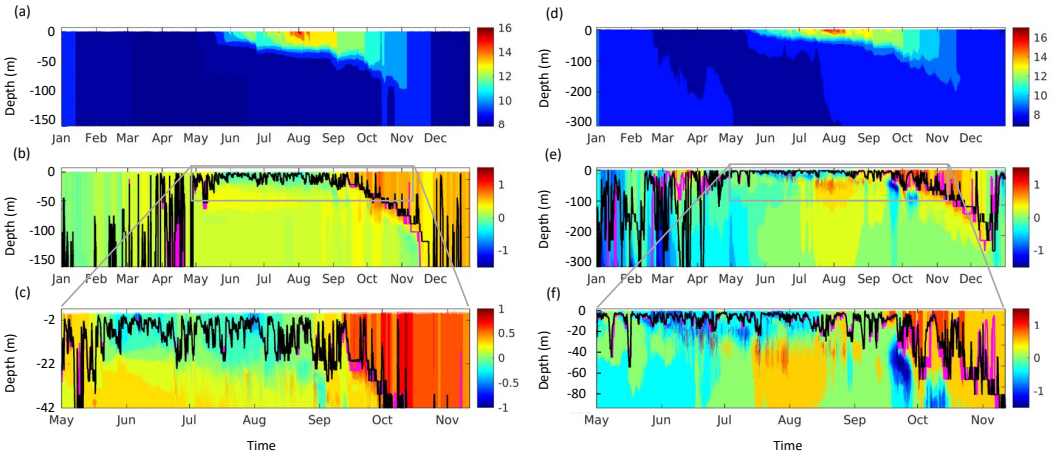

Figure 10. (a) The annual variation of temperature and (b) the differences (DA Run - Free Run) in the middle of the Shetland Shelf transect, and (c) shows the zoom-in of (b) near the surface during summer. The right column is similar to the left, but for the middle of the Norwegian Channel transect. In panels (b), (c), (e) and (f) magenta and black lines denote the locations of the mixing layer depth of the Free Run and DA Run, respectively.

4.3 Physical processes that induce advective transport

The results presented in Section 3.2 reveal that the assimilation of SST data would affect hydrodynamic processes, which consequently induces volume transport and causes lateral transport and redistribution of heat. To gain a better understanding of the impacts of DA on these processes, the current velocities and local areas along the five selected transects are decomposed by applying a tidal harmonic analysis (Pawlowicz et al., 2002):

$$u_{\mathrm{n}} = \overline{u}_{\mathrm{n}} + u_{\mathrm{n}}^{\mathrm{t}} + u_{\mathrm{n}}^{\mathrm{w}}, \tag{14}$$

$$\mathrm{d}A_{\mathrm{n}} = \overline{\mathrm{d}A}_{\mathrm{n}} + \mathrm{d}A_{\mathrm{n}}^{\mathrm{t}} + \mathrm{d}A_{\mathrm{n}}^{\mathrm{w}}. \tag{15}$$

Here, an overbar represents an annual average, and a superscript "t" indicates a harmonic quantity with zero mean that consists of multiple tidal components. Moreover, "w" denotes an irregular time-varying quantity that is regarded as the result of wind stress or nonlinear processes. Thus, the annual mean volume transport is separated into components due to different physical processes:

$$\overline{q^{\mathrm{V}}} = \underbrace{\int_A \overline{u}\,\overline{\mathrm{d}A}}_{\text{Eulerian}} + \underbrace{\int_A \overline{u^{\mathrm{t}}\,\mathrm{d}A^{\mathrm{t}}}}_{\text{Stokes}} + \underbrace{\int_A \overline{u^{\mathrm{w}}\,\mathrm{d}A^{\mathrm{w}}}}_{\text{Wind}} + \underbrace{\int_A \overline{u^{\mathrm{t}}\,\mathrm{d}A^{\mathrm{w}}} + \int_A \overline{u^{\mathrm{w}}\,\mathrm{d}A^{\mathrm{t}}}}_{\text{Wind-tide interaction}}. \tag{16}$$

The physical meanings of the terms on the right-hand side of eq. 16 can be considered as follows: the first term is the Eulerian residual volume transport, which is related to the annual mean baroclinic pressure gradient, wind stress, nonlinear advection, etc.; the second term represents Stokes transport, the third term is attributable to wind fluctuations; and the remaining terms are nonlinear correlations of tides and wind. Similarly, $T_k = \overline{T_k} + T_k'$, i.e., the annual average and fluctuating terms and the advective heat transport, are decomposed as well:

$$\begin{aligned}
\overline{q^{\mathrm{H}}} \;=\; & \Big(\underbrace{\int_A \overline{T_k}\,\overline{u}\,\overline{\mathrm{d}A}}_{\text{Eulerian}} + \underbrace{\int_A \overline{T_k}\,\overline{u^{\mathrm{t}}\,\mathrm{d}A^{\mathrm{t}}}}_{\text{Stokes}} + \underbrace{\int_A \overline{T_k}\,\overline{u^{\mathrm{w}}\,\mathrm{d}A^{\mathrm{w}}}}_{\text{Wind}} + \\
& \underbrace{\int_A \overline{T_k'\,u^{\mathrm{t}}}\,\overline{\mathrm{d}A} + \int_A \overline{T_k'\,\mathrm{d}A^{\mathrm{t}}}\,\overline{u} + \int_A \overline{T_k'\,\mathrm{d}A^{\mathrm{t}}\,u^{\mathrm{t}}}}_{\text{Tidal pumping}} + \\
& \underbrace{\int_A \overline{T_k'\,u^{\mathrm{w}}}\,\overline{\mathrm{d}A} + \int_A \overline{T_k'\,\mathrm{d}A^{\mathrm{w}}}\,\overline{u} + \int_A \overline{T_k'\,\mathrm{d}A^{\mathrm{w}}\,u^{\mathrm{w}}}}_{\text{Wind pumping}} + \\
& \underbrace{\int_A \overline{T_k}\,\overline{u^{\mathrm{t}}\,\mathrm{d}A^{\mathrm{w}}} + \int_A \overline{T_k}\,\overline{u^{\mathrm{w}}\,\mathrm{d}A^{\mathrm{t}}} + \int_A \overline{T_k'\mathrm{d}A^{\mathrm{t}}\,u^{\mathrm{w}}} + \int_A \overline{T_k'\,\mathrm{d}A^{\mathrm{w}}\,u^{\mathrm{t}}}}_{\text{Wind-tide interaction}}\Big)\,c_p\,\rho.
\end{aligned} \tag{17}$$

In eq. 17, two additional terms occur, which are related to transports caused by tidal pumping and wind pumping. The former is due to the correlation between seawater temperature fluctuations and tides, while the latter is due to the correlation between seawater temperature fluctuations and wind.

As shown in Figure 11a, along all the transects throughout the North Sea, the main contribution to volume exchange is Eulerian transport. Stokes transport, which results from the correlation between strong tidal currents and tidal waves distorted by bottom friction, also plays an important role at the Dover Strait (contributing approximately 0.04 Sv). Along all the remaining transects, Stokes transport, wind and wind-tide interactions are weak. The decomposition results reveal a large difference between the Free Run and DA Run at the Norwegian Channel due to the strong reduction in Eulerian transport. Moreover, regard to heat advection (Figure 11b), Stokes transport is as significant as Eulerian transport through the Dover Strait. At the Fair Isle and the Shetland Shelf,

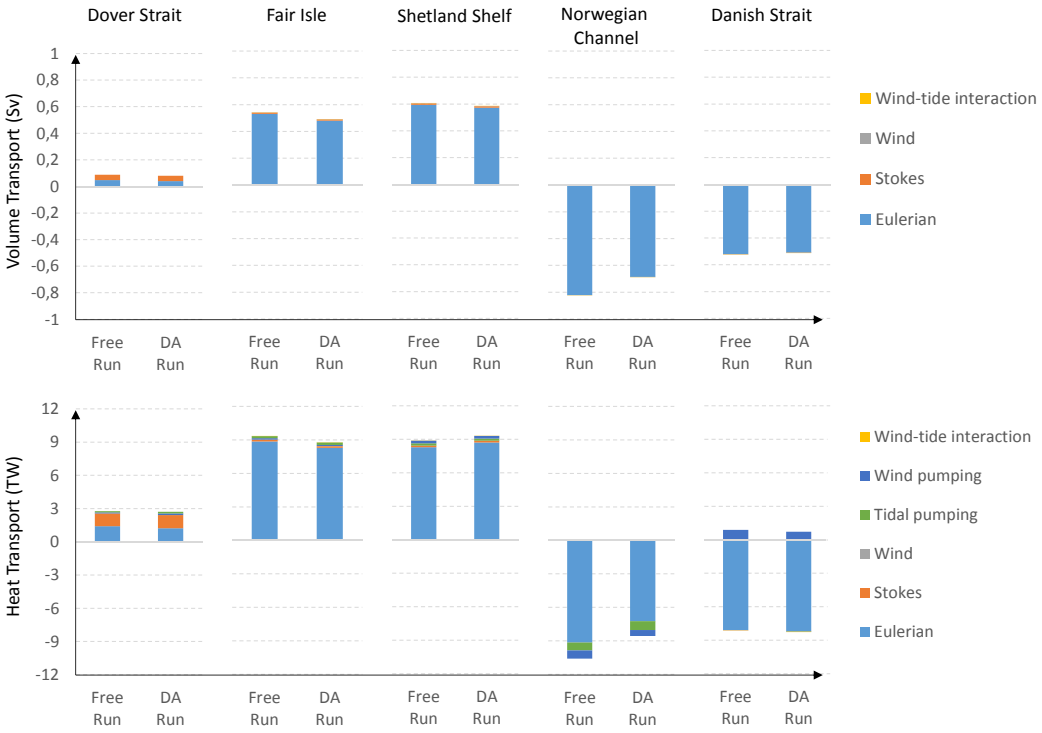

Figure 11. The annual mean transport of (a) volume and (b) heat due to different physical processes at the five selected transects. Positive/negative values denote fluxes inward/outward the North Sea.

the net transport into the North Sea due to the annual mean current is an order of magnitude larger than that due to the other processes. Similarly, at the Norwegian Channel, the largest contribution also comes from the annual mean current, followed by tidal pumping and wind pumping. Note that wind pumping is negligible in the Danish Strait but plays a role opposite to Eulerian transport. Similar to the results of the volume decomposition, at the Norwegian Channel, DA largely reduces heat transport by the annual mean current.

Because the atmospheric forcing is prescribed, changes in the annual mean wind stress are not considered. The main differences in Eulerian transport between the Free Run and DA Run are attributed to the modification of the following components: a) spatial variations in the heating or cooling of the surface lead to changes in pressure gradients, and b) heating of the surface leads to increased stability of the water column and hence reduced internal friction. Due to the assimilation of SST data, the pressure gradient from the North Sea towards the North Atlantic declines. Figure 12 shows the annual mean

sea surface height (SSH) difference and density difference between the DA Run and the Free Run along the Norwegian Mouth transect (see Figure 1). A high correlation is observed between the two terms, and the water density inside the Norwegian Channel (at distances of less than 100 km, Figure 12b) is reduced, while the density near the shelf edge is increased(120 km $\sim$ 200 km, Figure 12b). Furthermore, as mentioned in the previous section, an inward current from the Atlantic to the North Sea exists along the western side of the Norwegian Channel transect; t current represents a branch of the eastward along-shelf current in the Atlantic. In Figure 13, the arrows with length and direction reflect the vertical mean current averaged over monthly periods (hence, the dominant tidal components are removed, e.g., M_2) for the different seasons of 2017. The contours indicate the difference in the velocity intensity between the DA Run and the Free Run, where red (positive values) refer to the enhancement of the current due to the assimilation of SST data, while blue (negative values) indicates weakening of the current. This figure clearly shows that the current in the Atlantic is enhanced along the northern side of the North Sea shelf because of the SST assimilation (denoted by the yellow arrow in Figure 13, especially in winter and spring (Figure 13a and b)). As a result, the branch current along the western side of the Norwegian Channel increases persistently over the whole year. Such enhanced inflow compensates for the net outward flow of the North Sea. Furthermore as shown by the blue and red patterns with length scales of approximately 10 to 20 km in the Norwegian Channel (e.g., Figure 13a and c), the changes in current field present rather complex patterns in the Norwegian Channel. This implies that DA could also impact the internal Rossby radius, which has a similar spatial scale to these blue/red pattern in that area (Holt & Proctor, 2008).

5 Conclusions

The present study investigated the impact of the assimilation of satellite SST data on the simulation of the volume and heat budgets for the North Sea in a wave-circulation coupled system. This work follows that by Lewis et al. (2019), who showed that model coupling alone is not a sufficient strategy for improving all aspects of model performance. The 3DVAR scheme is implemented with the assumption that the model SST errors are strongly correlated with the temperature errors inside the mixing layer. This work demonstrates that the assimilation of OSI SAF SST data can improve the model analysis results, with reducing the RMSE from 0.7°C $\sim$ 1.8°C to 0.3°C $\sim$ 0.9°C. In general, with

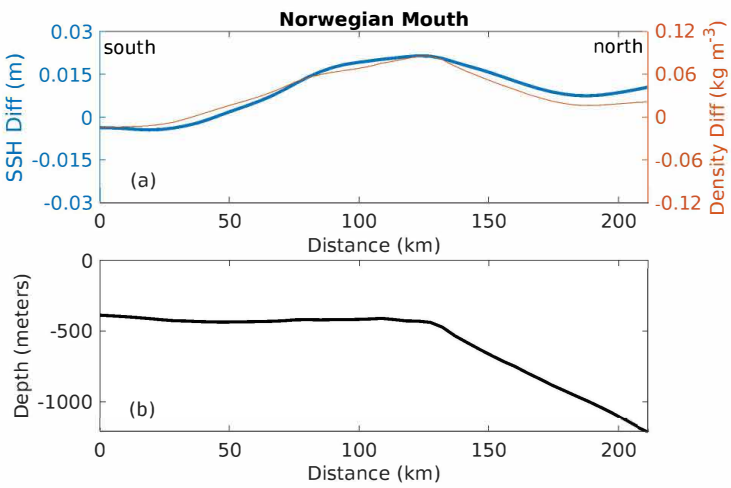

Figure 12. (a) The annual mean SSH and density difference (DA Run − Free Run), and (b) the water depth along the transect 6 in the Norwegian trench as shown in Figure 1.

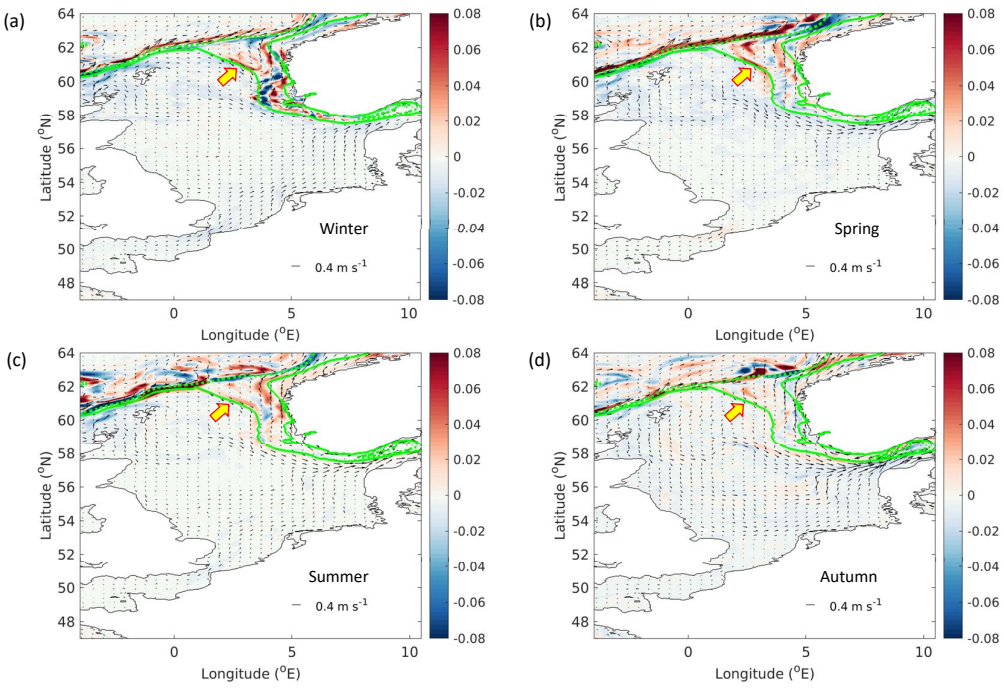

Figure 13. The vertical mean current averaged over one month periods in 2017 for (a) February of winter, (b) April of spring, (c) July of summer and (d) November of autumn, respectively. Arrows are velocities of the DA Run and the contours denote the differences in velocity intensity between the two model runs (i.e., abs(u_{DA}) − abs(u_{Free})). Positive (negative) values represent the increasing (decreasing) of the velocity due to DA. Solid and dotted lines in green indicate the sea bottom of 250 m and 500 m, respectively.

DA, the surface temperature in the North Sea increases by approximately 0.5°C $\sim$ 1.2°C. Further comparison of the analyzed model results with independent profile observations shows improvements in the seawater temperature at deeper water layers. At two MARNET stations NSB-III and FINO 1, the differences (1.0°C $\sim$ 1.5°C) between the observations and the Free Run at moderate water depths and near the bottom are corrected by the assimilation.

The total lateral advective volume and heat transports of the DA Run are decomposed into terms that are induced by the individual responses of physical quantities and their interactions with the assimilation. These quantities include the current velocity, sea surface elevation and water temperature. With the DA, both the inward and the outward volume transport, and consequently the lateral heat transport of the North Sea are decreased. The main difference in the volume transport between the Free Run and the DA Run is due to the current velocity changes induced by the assimilation of SST data. This term counteracts the Free Run volume transport and has the largest impact on the Norwegian Channel among all five open boundary transects crossing the North Sea.

The current field changes due to SST assimilation further affect the lateral heat transport. The decreased volume transport through the Norwegian Channel yields a better water mass balance over the North Sea and thus a net heat gain with reduced error. Moreover, the sensitivity study regarding the reference temperature, reveals that the North Sea had a net heat gain through lateral advection in 2017 with the annual mean flux of 4.7 ± 0.5 TW. As another main component of the heat budget of the North Sea, the air-sea heat exchange is enhanced due to SST assimilation. The results show that the heat flux from sea to air increases by 39 % (from 7.97 TW to 11.08 TW) over the entire domain. This is attributed to the direct local temperature correction by DA and the indirect impact from the non-local temperature correction and heat transport by lateral advection.

Further analysis of the advective heat exchange induced by individual physical processes reveals that Eulerian transport is the dominant mechanism in the north (along the Fair Isle, Shetland Shelf, and Norwegian Channel transect) and the east (the Danish Strait transect) open boundaries of the North Sea. In the west (the Dover Strait transect), Stokes transport is as important as Eulerian transport. At the Norwegian Channel and the Danish Strait, heat transport due to tidal pumping has a second-order contribution to the

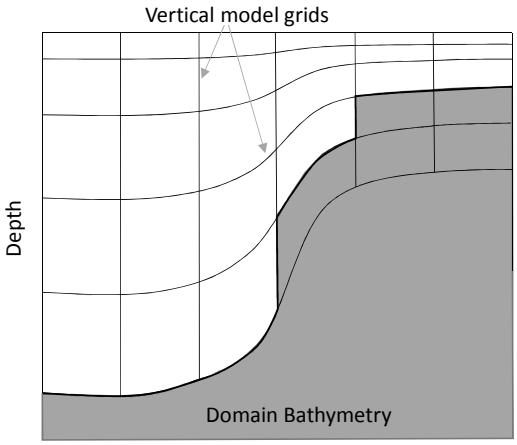

Figure A1. Sketch of the σ-z^* hybrid grid use in NEMO model.

total heat exchange, whereas, transport induced by the annual mean wind stress, wind pumping and wind-tide interactions is rather small. SST assimilation decreases the horizontal density gradients from the North Sea to the Atlantic and causes changes in the velocity field within the Norwegian Channel and in turn reduces the Eulerian transport of of water and heat.

This study contributes to the improvement of tools to better quantify different components of the heat budget of the North Sea. With the growing debate regarding the impacts of climate change on the North Sea, accurate assessments of these factors will be of increasing importance in the future.

Appendix A NEMO-WAM setup

A side view of the σ-z^* hybrid grid is sketched in Figure A1. The standard NEMO hybrid grid features tangential stretching below a depth of 200 m. The minimum water depth of the model is 8 m, and the maximum depth is 6300 m. This grid configuration results in a minimum level thickness of 0.16 m at the surface and a maximum level thickness of 755 m at the bottom. The model uses a nonlinear free sea surface with a variable volume. The barotropic subcycle time step is adaptively determined during the run time using a maximum Courant number of 0.8. The solution of the barotropic subcycle is filtered using a box filter, and the hydrostatic pressure gradient is estimated using the σ-coordinate pressure Jacobian scheme.

721 The advection of momentum conserves both energy and enstrophy, and a bi-Laplacian
722 horizontal diffusion operator with a coefficient of -2.8×10^{-8} m^4s^{-1} is applied. The free-
723 slip lateral boundary condition is employed for momentum along the coastline. A spa-
724 tially varying logarithmic layer is adopted for the bottom friction with a bottom rough-
725 ness length of 1×10^{-6} m for the Danish Straits and the Baltic Sea and 4×10^{-3} m
726 for the rest of the domain. Tracer advection uses a total variation diminishing (TVD)
727 approach with the total variance decreasing scheme described in Zalesak (1979). Tracer
728 advection is parameterized by the TVD scheme and a 2D varying Laplacian diffusion op-
729 erator with a value of 0.25 m^2s^{-1} for the region covering the Danish Straits and the Baltic
730 Sea and a value of 50 m^2s^{-1} for the rest of the domain. Lateral diffusion for the trac-
731 ers is applied along with geopotential levels. In the vertical direction, the Craig and Ban-
732 ner surface wave mixing parameterization (Craig & Banner, 1994) is applied with a wave
733 breaking TKE flux constant of 150, and the dissipation under stratification is limited us-
734 ing a Galperin limit of 0.07 (Galperin et al., 1988).

735 The lateral boundary forcing uses the NEMO "BDY" standard. The boundary forc-
736 ing for the tracers (temperature and salinity) is derived from the hourly Copernicus Ma-
737 rine Environment Monitoring Service (CMEMS) Forecast Ocean Assimilation Model (FOAM)
738 Atlantic Margin Model version 7 (AMM7) output (O'Dea et al., 2012), which is inter-
739 polated over the model grid and applied as hourly interpolated vertical profiles at the
740 lateral boundaries using the flow relaxation scheme (FRS) (Engerdahl, 1995; David, 1976).
741 The boundary forcing for water levels and currents is split into three components: a tidal
742 harmonic signal, a barotropic signal and a baroclinic anomaly profile. The tidal harmonic
743 forcing is reconstructed for each model time-step from the tidal constituents for the M2,
744 S2, N2, K2, K1, O1, Q1, P1 and M4 constituents derived from the TPXOv8 model (OSU-
745 OTIS). The barotropic forcing consists of the tidally averaged sea surface elevation and
746 depth mean currents and is derived from hourly CMEMS FOAM AMM7 output. The
747 baroclinic forcing is the anomaly of the current profile with respect to the combined tidal
748 and barotropic signal. The Flather radiation scheme (FRS) (Flather, 1994) is used for
749 the tidal harmonic and barotropic forcing at the first lateral boundary bin of the model.
750 The baroclinic forcing uses the FRS. In additional to the lateral tidal forcing, a tidal po-
751 tential forcing with the same tidal constituents is applied over the whole model domain.

752 Atmospheric forcing is introduced into the model using the NEMO CORE bulk for-
753 mulation (Large & Yeager, 2004) and hourly atmospheric forcing fields, which are de-

rived from the European Centre for Medium-Range Weather Forecasts (ECMWF) Reanalysis version 5 (ERA5) data set and consist of 10 m wind components, 2 m temperature and dew-point temperature, mean sea level pressure, and downward solar and thermal radiations. The penetrative solar radiation scheme uses a 2-band approach with the Jerlov water classification type IV parameterization (abs = 0.8, si0 = 0.9, and si1 = 2.10). Surface freshwater input is provided by the ERA5 hourly snowfall and total precipitation in addition to a processed daily river climatology based on river discharge data sets derived from BSHE-HYPE and Met-Oce

Acknowledgments

The study is supported by the Advanced Earth System Modelling capacity (ESM, `https://www.esm-project.net/`) project (funded by the German Helmholtz Association (HGF)). The authors gratefully acknowledge Jülich Supercomputing Centre (JSC) for providing computing time on the Supercomputer JUWELS. J.Schulz-Stellenfleth and J. Staneva acknowledge support from the Project "OceanCurrents" (Nr. 03F0822A) funded by the Federal Ministry of Education and Research (BMBF). The data from the simulations and observation measurements are available online at the HZG repository with `https://coastmap.hzg.de/coastmap/maps/data/JGR/JGR_Data_source.zip`.

References

Alari, V., Staneva, J., Breivik, Ø., Bidlot, J.-R., Mogensen, K., & Janssen, P. (2016). Surface wave effects on water temperature in the Baltic Sea: simulations with the coupled NEMO-WAM model. *Ocean Dynamics*, *66*, 917-930. doi: 10.1007/s10236-016-0963-x

Annan, J. D., & Hargreaves, J. C. (1999). Sea surface temperature assimilation for a three-dimensional baroclinic model of shelf seas. *Continental Shelf Research*, *19*, 1507-1520. doi: 10.1016/S0278-4343(99)00033-3

Bidlot, J. R., Janssen, P. A. E. M., & Abdalla, S. (2007). *A revised formulation of ocean wave dissipation and its model impact*. ECMWF.

Canuto, V. M., Howard, A., Cheng, Y., & Dubovikov, M. S. (2001). Ocean turbulence. part i: One-point closure model-momentum and heat vertical diffusivities. *Journal of Physical Oceanography*, *31*, 1413-1426.

Craig, P. D., & Banner, M. L. (1994). Modelling wave enhanced turbulence in the

ocean surface layer. *Journal of Physical Oceanography*, *24*, 2546-2559. doi: 10.1175/1520-0485(1994)⟨2546:MWETIT⟩2.0.CO;2

Danielssen, D. S., Edler, L., Fonselius, S., Hernroth, L., Ostrowski, M., Svendsen, E., & Talpsepp, L. (1997). Oceannographic variability in the Skagerrak and Northern Kattegat, May-June, 1990. *Journal of Marine Science*, *54*, 753-773. doi: 10.1006/jmsc.1996.0210

David, H. (1976). A lateral boundary formulation for multi-level prediction models. *Quarterly Journal of the Royal Meteorological Society*, *102*, 405-418. doi: 10.1002/qj.49710243210

Dieterich, C., Wang, S., Schimanke, S., Gröger, M., Klein, B., Hordoir, R., ... others (2019). Surface heat budget over the North Sea in climate change simulations. *Atmosphere*, *10*(5), 272. doi: 10.3390/atmos10050272

Dobricic, S., Pinardi, N., Adani, M., Bonazzi, A., Fratianni, C., & Tonani, M. (2005). Mediterranean Forecasting System: An improved assimilation scheme for sea-level anomaly and its validation. *Quarterly Journal of the Royal Meteorological Society*, *131*(613), 3627–3642.

Dye, S., Hughes, S. L., Tinker, J., Berry, D. I., Holliday, N. P., Kent, E. C., ... others (2013). Impacts of climate change on temperature (air and sea). MCCIP Secretariat.

Engerdahl, H. (1995). Use of the flow relaxation scheme in a three-dimensional baroclinic ocean model with realistic topography. *Tellus*, *47A*, 365-382. doi: 10.1034/j.1600-0870.1995.t01-2-00006.x

Fallmann, J., Lewis, H., Castillo, J. M., Arnold, A., & Ramsdale, S. (2017). Impact of sea surface temperature on stratiform cloud formation over the north sea. *Geophysical Research Letters*, *44*(9), 4296–4303.

Flather, R. (1994). A storm surge prediction model for the northern bay of bengal with application to the cyclone disaster in April 1991. *Journal of Physical Oceanography*, *24*, 172-190. doi: 10.1175/1520-0485(1994)024⟨0172:ASSPMF⟩2.0.CO;2

Fu, W., She, J., & Zhuang, S. (2011). Application of an Ensemble Optimal Interpolation in a North/Baltic Sea model: Assimilating temperature and salinity profiles. *Ocean Modelling*, *40*, 227-245. doi: 10.1016/j.ocemod.2011.09.004

Galperin, B., Kantha, L. H., Hassid, S., & Rosati, A. (1988). A quasi-equilibrium

turbulent energy model for geophysical flows. *Journal of the Atmospheric Sciences*, *45*, 55-62.

Grayek, S., Stanev, E. V., & Schulz-Stellenfleth, J. (2015). Assessment of the Black Sea observing system. A focus on 2005-2012 Argo campaigns. *Ocean Dynamics*, *65*, 1665-1684. doi: 10.1007/s10236-015-0889-8

Günther, H., Hasselmann, S., & Janssen, P. A. E. M. (1992). *The WAM model, Cycle 4.* Haumburg.

Hersbach, H., & Janssen, P. A. E. M. (1999). Improvement of the Short-Fetch Behavior in the Wave Ocean Model (WAM). *Journal of Physical Oceanography*, *16*, 884–892. doi: 10.1175/1520-0426(1999)016⟨0884:IOTSFB⟩2.0.CO;2

Hjøllo, S. S., Skogen, M. D., & E., S. (2009). Exploring currents and heat within the North Sea using a numerical model. *Journal of Marine Systems*, *78*, 180-192. doi: 10.1016/j.jmarsys.2009.06.001

Ho-Hagemann, H., Hagemann, S., Grayek, S., Petrik, R., Rockel, B., Staneva, J., ... Schrum, C. (2020). Internal Model Variability of the Regional Coupled System Model GCOAST-AHOI. *Atmosphere*, *11*, 1–36. doi: 10.3390/atmos11030227

Holt, J., & Proctor, R. (2008). The seasonal circulation and volume transport on the northwest European continental shelf: A fine-resolution model study. *Journal of Geophysical Research*, *113*, C06021. doi: 10.1029/2006JC004034

Huthnance, J. M., Holt, J. T., & Wakelin, S. L. (2009). Deep ocean exchange with west-european shelf seas. *Ocean Science*, *5*, 621–634.

Janssen, P. A. E. M. (2008). Progress in ocean wave forecasting. *Journal of Computational Physics*, *227*, 3572–3594. doi: 10.1016/j.jcp.2007.04.029

Kirby, R. R., Beaugrand, G., Lindley, J. A., Richardson, A. J., Edwards, M., & Reid, P. C. (2007). Climate effects and benthic–pelagic coupling in the north sea. *Marine Ecology Progress Series*, *330*, 31–38.

Kjellström, E., Döscher, R., & Meier, H. M. (2005). Atmospheric response to different sea surface temperatures in the baltic sea: coupled versus uncoupled regional climate model experiments. *Hydrology Research*, *36*(4-5), 397–409.

Knight, J. R., Allan, R. J., Folland, C. K., Vellinga, M., & Mann, M. E. (2005). A signature of persistent natural thermohaline circulation cycles in observed climate. *Geophysical Research Letters*, *32*(20).

Komen, G. J., Cavaleri, L., M., D., Hasselmann, K., Hasselmann, S., & Janssen,

P. A. E. M. (1994). *Dynamics and modelling of ocean waves.* Cambridge: Cambridge University Press.

Large, W. G., & Yeager, S. (2004). *Diurnal to decadal global forcing for ocean and sea-ice models: the data sets and flux climatologies* (Tech. Rep.). CGD Division of the National Center for Atmospheric Research. (NCAR Technical Note, NCAR/TN-460+STR)

Lewis, H. W., Castillo Sanchez, J. M., Siddorn, J., King, R. R., Tonani, M., Saulter, A., ... Bricheno, L. (2019). Can wave coupling improve operational regional ocean forecastes for the north-west European Shelf? *Ocean Science*, *15*, 669–690. doi: 10.5194/os-15-669-2019

Liu, Y., Zhu, J., She, J., Zhuang, S., Fu, W., & Gao, J. (2009). Assimilating temperature and salinity profile observations using an anisotropic recursive filter in a coastal ocean model. *Ocean Modelling*, *30*(2-3), 75–87.

Lorenc, A. C. (1997). Development of an operational variational assimilation scheme (gtspecial issueltdata assimilation in meteology and oceanography: Theory and practice). *Journal of the Meteorological Society of Japan. Ser. II*, *75*(1B), 339–346.

Losa, S. N., Danilov, S., J., S., Nerger, L., Maßmann, S., & Janssen, F. (2012). Assimilating NOAA SST data into the BSH operational circulation model for the North and Baltic Seas: Inference about the data. *Journal of Marine Science*, *105-108*, 152-162. doi: 10.1016/j.jmarsys.2012.07.008

Losa, S. N., Danilov, S., Schröter, T., Jens an d Janjić, Nerger, L., & Janssen, F. (2014). Assimilating NOAA SST data into BSH operational circulati on model for the North and Baltic Seas: Part 2. Sensitivity of the for ecast's skill to the prior model error statistics. *Journal of Marine Systems*, *129*, 259–270.

Madec, G., & the NEMO team. (2006). *Nemo ocean engine, note du pole de modélisation.* France: Institut Pierre-Simon Laplace (IPSL) No. 27. ISSN-1288-1619.

NOOS. (2010). *NOOS Activity Exchange of computed water, salt, and heat transports across selected transects. North West European Shelf Operational Oceanographic System (NOOS).* Retrieved from `https://www.baltic.earth/organisation/bewg_coupledmod/Mallorca_2018/exch_transports_NOOS-BOOS_2010-11-11.pdf`

Otto, L., Zimmerman, J. T. F., Furnes, G. K., Mork, M., Sætre, R., & Becker, G. (1990). Review of the physical oceanography of the North Sea. *Netherlands Journal of Sea Research*, *26*, 161-238. doi: 10.1016/0077-7579(90)90091-T

O'Dea, E. J., Arnold, A. K., Edwards, K. P., Furner, R., Hyder, P., Martin, M. J., ... Liu, H. (2012). An operational ocean forecast system incorporating nemo and sst data assimilation for the tidally driven european north-west shelf. *Journal of Operational Oceanography*, *5*, 3-17. doi: 10.1080/1755876X.2012.11020128

Pawlowicz, R., Beardsley, B., & Lentz, S. (2002). Classical tidal harmonic analysis including error estimates in matlab using T_TIDE. *Computers and Geosciences*, *28*, 929-937. doi: 10.1016/S0098-3004(02)00013-4

Prandle, D., Ballard, G., Flatt, D., Harrison, A. J., Jones, S. E., Knight, P. J., ... Tappin, A. (1996). Combining modelling and monitoring to determine fluxes of water, dissolved and particulate metals through the Dover Strait. *Continental Shelf Research*, *16*, 237-257. doi: 10.1016/0278-4343(95)00009-P

Quante, M., & Colijn, F. (2016). *North sea region climate change assessment.* SpringerOpen.

Schrum, C., & Backhaus, J. O. (1999). Sensitivity of atmosphere–ocean heat exchange and heat content in the north sea and the baltic sea. *Tellus A*, *51*(4), 526–549.

Staneva, J., Alari, V., Breivik, O., Bidlot, J. R., & Mogensen, K. (2017). Effects of wave-induced forcing on a circulation model of the North Sea. *Ocean Dynamics*, *67*, 81–191. doi: 10.1007/s10236-016-1009-0

Staneva, J., Behrens, A., Gayer, G., & Aouf, L. (2019). Synergy between CMEMS products and newly available data from SENTINEL. In K. von Schuckmann & P.-Y. L. Traon (Eds.), *Copernicus marine service ocean state report, issue 3* (chap. 3.3). doi: 10.1080/1755876X.2019.1633075

Staneva, J., Schrum, C., Behrens, A., Grayek, S., Ho-Hagemann, H., Alari, V., ... Bidlot, J. R. (2018). A North Sea-Baltic sea regional coupled models: atmosphere, wind waves and ocean. In E. Buch, V. Fernández, D. Eparkhina, P. Gorringe, & G. Nolan (Eds.), *Operational oceanography serving sustainable marine development* (p. 516).

Staneva, J., Wahle, K., Günther, H., & Stanev, E. (2016). Coupling of wave and

circulation models in coastal–ocean predicting systems: a case study for the German Bight. *Ocean Science*, *12*, 797–806. doi: 10.5194/os-12-797-2016

The Wamdi Group. (1988). The WAM Model—A Third Generation Ocean Wave Prediction Model. *Journal of Physical Oceanography*, *18*, 1775–1810. doi: 10 .1175/1520-0485(1988)018⟨1775:TWMTGO⟩2.0.CO;2

Umlauf, L., & Burchard, H. (2003). A generic lengthscale equation for geophysical turbulence models. *Journal of Marine Research*, *61*, 235-265. doi: 10.1357/ 002224003322005087

Winther, N. G., & Johannessen, J. A. (2006). North Sea circulation: Atlantic inflow and its destination. *Journal of Geophysical Research*, *111*, C12018. doi: 10.1029/2005JC003310

Wu, L., Staneva, J., Breivik, O., Rutgersson, A. J., A. adn George Nurser, Clementi, E., & Madec, G. (2019). Wave effects on coastal upwelling and water level. *Ocean Modelling*, *140*, 101405. doi: 10.1016/j.ocemod.2019.101405

Zalesak, S. T. (1979). Fully multidimensional flux-corrected transport algorithms for fluids. *Journal of Computational Physics*, *31*, 335-362.